



HAL
open science

Augmented Depolarizing Scatterer Based on Resonant Elements For Polarimetric Radar Calibration

Zeshan Ali, Etienne Perret

► **To cite this version:**

Zeshan Ali, Etienne Perret. Augmented Depolarizing Scatterer Based on Resonant Elements For Polarimetric Radar Calibration. IEEE Transactions on Antennas and Propagation, 2022, 70 (2), pp.1415-1427. 10.1109/TAP.2021.3111283 . hal-03353064

HAL Id: hal-03353064

<https://hal.science/hal-03353064>

Submitted on 23 Sep 2021

HAL is a multi-disciplinary open access archive for the deposit and dissemination of scientific research documents, whether they are published or not. The documents may come from teaching and research institutions in France or abroad, or from public or private research centers.

L'archive ouverte pluridisciplinaire **HAL**, est destinée au dépôt et à la diffusion de documents scientifiques de niveau recherche, publiés ou non, émanant des établissements d'enseignement et de recherche français ou étrangers, des laboratoires publics ou privés.

Augmented Depolarizing Scatterer Based on Resonant Elements For Polarimetric Radar Calibration

Zeshan Ali and Etienne Perret, *Senior Member, IEEE*

Abstract—A 3-in-1 depolarizing circular scatterer for the polarimetric radar calibration is proposed in this paper. The proposed scatterer is low cost, compact, planar circuit, and well suited for the radar operating in a compact range, for example, chipless RFID technology. By the virtue of its circular shape, the rear side of the proposed scatterer acts as a metallic disk with strong co polarization backscattered signals. The front side is composed of eight resonant dipoles which make it nondepolarizing and depolarizing scatterers at the inclination of 0° and 45° , respectively. The features of proposed circular scatterer are tested as reference calibration objects for single antenna based polarimetric radar calibration techniques. Two test objects are utilized: a dihedral tilted at 45° and a depolarizing multi resonant planar structure commonly called chipless RFID tag. The performance of proposed circular scatterer is also compared with the standard reference calibration objects: a metallic disk and a dihedral tilted at 22.5° . The performance of proposed circular scatterer is comparable to the standard reference calibration objects for the calibration techniques (namely Type 1 and Type 2). The proposed scatterer is potentially tolerant of displacement up to 1 cm and misalignment equals 2° .

Index Terms—Calibration technique, polarimetric radar, radar cross section, scatterer.

I. INTRODUCTION

POLARIMETRIC radars are also referred to as dual-polarization radars, as they can transmit and receive simultaneously over both vertical V and horizontal H polarizations. This dual-polarization behavior leads to antenna cross-polarization couplings. The conventional radar cross section (RCS) calibration approach does not take into account such cross polarization couplings (see [1], eq. (2)). For accurate calibration of polarimetric radar, such cross polarization illumination errors should also be taken into account [2]. In the literature, numerous full polarimetric radar calibration procedures are proposed [1]–[6]. Generally, for full

polarimetric calibration, at least two calibration scatterers (or at least two alignments of a depolarizing calibration scatterer) are needed. For example, common planar calibration scatterers are metallic plate [7], metallic circular disk [8], whereas the common 3D calibration scatterers are wire mesh [4], [8], [9], metallic sphere [8], [10], metallic cylinder [8], dihedral [3], [7], [8], and trihedral [7], [8]. The cylinder, the dihedral, the trihedral, and the wire mesh are depolarizing objects.

In this paper, an augmented depolarizing circular scatterer is proposed for the full calibration of polarimetric radar. The proposed scatterer is composed of resonant dipoles. With the use of circular geometry and the resonant dipoles, the proposed scatterer presents a 3-in-1 behavior: 1) from the rear side, it behaves like a metallic disk; 2) from the front side with vertically aligned dipoles, it backscatters dominant co polarization signals; and 3) from the front side with 45° tilted dipoles, it backscatters strong cross polarization signals along with co polarization signals. Furthermore, the proposed scatterer is planar, compact, and realized by using low cost printed circuit board (PCB) technology. To the best of our knowledge, we present the first entirely planar 3-in-1 reference scatterer for polarimetric radar calibration. In contrast, usually, corner reflectors with large heights (dihedral and trihedral) are used for polarimetric radar calibration. Such a large height is a major limiting factor for these scatterers in terms of the radar range because their height should be compensated. The proposed scatterer is advantageous only for the systems that are forced to mimic the farfield measurements in the radiative near field (Fresnel region), for example, chipless radio frequency (RF) identification (RFID) technology. Chipless RFID tags operate in compact radar ranges because of low signal to noise ratio (SNR) at higher distances. The details of chipless RFID technology can be seen in [11]. To decode the identification (ID) encoded in the magnitude of RCS, a precise estimation of RCS of a chipless RFID tag is required [12].

The organization of this paper is as follows. Section III outlines the experimental methodology. Section III presents the polarimetric radar measurement setup. Section IV presents the design, realization, and simulations of the proposed circular scatterer and the other supplementary scatterers. Section V presents the procedures of the radar calibrations. Section VI presents the measurement results of the radar calibration and the uncertainty analyses of the proposed

This work was supported by the European Research Council (ERC) through the European Union's Horizon 2020 Research and Innovation Program under Agreement 772539 (SCATTERERID).

Z. Ali is with the Univ. Grenoble Alpes, Grenoble INP, LCIS, 26000 Valence, France (e-mail: zeshan.ali@lcis.grenoble-inp.fr).

E. Perret is with the Univ. Grenoble Alpes, Grenoble INP, LCIS, 26000 Valence, France, and also with the Institut Universitaire de France, 75005 Paris, France.

scatterer. Section VII draws conclusions.

II. EXPERIMENTAL METHODOLOGY

This Section briefly summarizes the experimental approach including the objects that are used, the calibration types, and the mechanism of comparison.

The polarimetric radar measurement setup is presented for all the experimental measurements.

The calibration and the test objects are presented: 1) proposed augmented depolarizing scatterer; 2) a metallic disk; 3) a dihedral; and 4) a chipless RFID tag. The metallic disk and the dihedral tilted at 22.5° are referred to as standard calibration set. The purpose of this standard calibration set is to make a point of reference for comparison with the performance of the proposed augmented calibration scatterer. On the other hand, the dihedral tilted at 45° and the chipless RFID tag are used as the test targets. These objects are used to determine the performances of both the proposed augmented scatterer and the standard calibration set.

A single antenna based polarimetric radar calibration technique is used for the radar calibration results. This technique is taken from [4] and referred to as calibration Type 1 in this paper. This calibration Type 1 is primarily dependent on the nondepolarizing object (that is, the rear side of the proposed scatterer or the metallic disk from the standard calibration set). We have derived a calibration Type 2 dependent on the depolarizing object (that is, the front side of the proposed scatterer tilted at 45° or the dihedral tilted at 22.5° from the standard calibration set). This calibration Type 2 is derived to show the limitations of the large height of the dihedral tilted at 22.5° from the standard calibration set.

The radar calibrations for the two test objects (the dihedral tilted at 45° and the chipless RFID tag) are calculated and compared using the standard calibration set as well as the proposed calibration scatterer for the calibration techniques Type 1 and Type 2. For each case of calibration objects, the calibration errors are calculated with respect to the simulated RCS signals of the test target. Also, the calibration errors for the proposed scatterer are calculated with respect to the calibrated signals from the standard calibration set. Finally, the proposed scatterer is characterized for the displacement and the rotational uncertainties.

III. POLARIMETRIC RADAR MEASUREMENT SETUP

The practical measurements of a scattering target with scattering matrix \mathbf{M}' from the polarimetric radar are modeled as found in [13]:

$$\mathbf{M}' = \mathbf{B} + \mathbf{RST} \quad (1)$$

where $\mathbf{S} = \begin{bmatrix} S_{VV} & S_{VH} \\ S_{HV} & S_{HH} \end{bmatrix}$ is the theoretical (or actual) scattering

matrix relating to the target under concern, $\mathbf{B} = \begin{bmatrix} B_{VV} & B_{VH} \\ B_{HV} & B_{HH} \end{bmatrix}$ is the background (clutter) scattering matrix, and $\mathbf{R} =$

$\begin{bmatrix} R_{VV} & R_{VH} \\ R_{HV} & R_{HH} \end{bmatrix}$ and $\mathbf{T} = \begin{bmatrix} T_{VV} & T_{VH} \\ T_{HV} & T_{HH} \end{bmatrix}$ are the distortion matrices (representing the effect of the antenna system or the multiplicative errors).

For the background normalized (i.e., with removed clutter) signals, (1) becomes:

$$\mathbf{M} = \mathbf{RST} \quad (2)$$

where $\mathbf{M} = \mathbf{M}' - \mathbf{B}$ is the background calibrated measured scattering matrix. For the rest of this paper, all measured signals are background normalized.

Fig. 1 shows the measurement setup with monostatic radar configuration inside an anechoic environment. For the conception of polarimetric radar system, Satimo QH800 dual polarization horn antenna (0.8 – 12 GHz) and Keysight P9375A vector network analyzer (VNA) are used, where the V and H polarized ports of the antenna are connected to the port 1 and port 2 of VNA. The cross polarization discrimination and port to port isolation of the employed antenna are larger than 30 dB with a range of gain 8 – 13 dBi within the employed frequency sweep range of 2 – 7 GHz [14]. The transmitting power delivered by VNA is -5 dBm. The objects are measured by placing them on a polystyrene quadpod in the center of main beam, where the antenna to scattering target distance is $d = 28$ cm. With $d = 28$ cm, both radar antenna and the calibration objects are in the Fresnel zones of each other. The Fresnel zone is considered because the proposed scatterer (composed of resonant dipoles) is intended for calibration of chipless RFID tags (composed of coupled resonant dipoles), where both the proposed scatterer and the chipless RFID tags might not be measured in farfield zone.

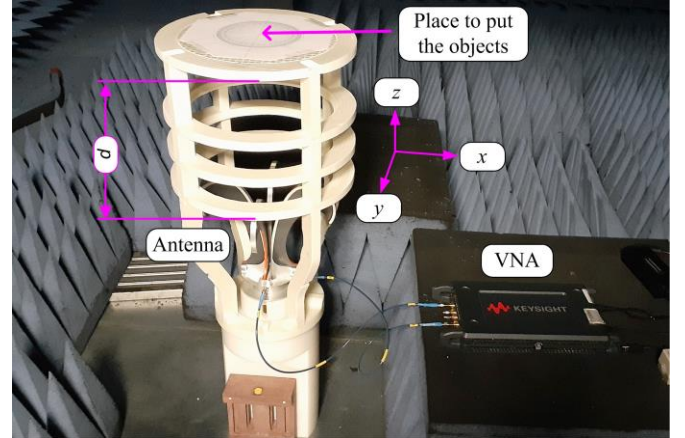


Fig. 1. Photograph of the measurement setup inside an anechoic environment.

IV. DESIGN, REALIZATION, AND SIMULATIONS OF THE SCATTERERS

Resonant dipoles are compatible (with a good compromise) with compact targets and capable to provide significant cross polarization signals. In addition, the resonant dipoles are lightweight planar structures that are very easy to fabricate using PCB technology. Conversely, the classical depolarizing reference objects (e.g., dihedral) are generally bulky and heavy structures. One advantage of the classical reference

objects is the naturally wideband response. On the other hand, the resonant dipoles exhibit a high SNR only around the frequency of resonance. The proposed calibration scatterer is composed of classical microstrip-based eight resonant dipoles of different frequencies of resonances to cover a wide band. These types of microstrip dipoles are modeled in [15]. The resonant signals backscattered from the proposed scatterer might not be directly incorporated in the radar calibration procedures. Thus, to utilize the proposed scatterer for the radar calibration, the fit signals will be used in the numerical calculations.

A. Proposed Calibration Scatterer

The front and rear view of the proposed calibration scatterer is presented in Fig. 2(a) and (b), respectively. The proposed scatterer is realized by utilizing the Rogers RO4003C substrate with dielectric permittivity $\epsilon_r = 3.55$, and substrate height $h = 0.81$ mm. The radius of the circular scatterer is $r = 7.4$ cm. The lengths of dipoles L_i are calculated using:

$$L_i = \frac{c}{2f_i\sqrt{\epsilon_{\text{eff}}}} \quad (3)$$

where f_i is the frequency of resonance of i th dipole. $\epsilon_{\text{eff}} = 2.80$ is the effective permittivity for the microstrip technology [16]. The first dipole L_1 is designed to resonate at 2.45 GHz for industrial, scientific, and medical (ISM) band. The subsequent dipoles $L_2, L_3, L_4, L_5, L_6, L_7,$ and L_8 resonate at 3 GHz, 3.5 GHz, 4 GHz, 4.5 GHz, 5 GHz, and 6 GHz, respectively, for ultra-wideband (UWB). After optimization during simulations, the lengths of dipoles L_i are $L_1=35.45$ mm, $L_2=28.79$ mm, $L_3=24.48$ mm, $L_4=21.27$ mm, $L_5=18.82$ mm, $L_6=16.82$ mm, $L_7=15.27$ mm, $L_8=13.88$ mm. The width of all dipole microstrips is $w=2$ mm. The dipoles are placed symmetrically with the separation between two consecutive dipoles $s = 1.5$ cm. The dipoles are arranged in an alternate fashion to reduce the coupling among consecutive resonators.

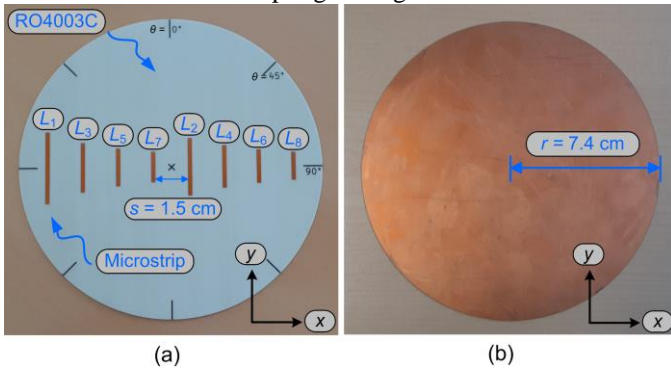


Fig. 2. Photographs of the proposed circular scatterer. (a) Front side view. (b) Rear side view.

Table I summarizes the three features of the proposed circular scatterer as the reference calibration objects. The proposed scatterer presents a 3-in-1 behavior: 1) circular disk scatterer from its rear side; 2) nondepolarizing scatterer from its front side aligned at 0° ; 3) depolarizing scatterer from its front side aligned at 45° .

TABLE I
THREE FEATURES OF THE PROPOSED CIRCULAR SCATTERER AS REFERENCE CALIBRATION OBJECTS

Feature	Side of the scatterer	Inclination of the scatterer	Scattering matrix
Target 1	Rear side	Any	$\begin{bmatrix} 1 & 0 \\ 0 & 1 \end{bmatrix}$
Target 2	Font side	0°	$\begin{bmatrix} a & 0 \\ 0 & b \end{bmatrix}$
Target 3	Font side	45°	$\begin{bmatrix} c & d \\ d & c \end{bmatrix}$

$a, b, c,$ and d are the components of the scattering matrices.

To estimate the ideal RCS signals of the objects, we have compared different solvers with plane wave excitation: frequency domain (FD) solver of HFSS, FD solver of CST and time domain (TD) solver of CST. We have found that the TD solver of CST presents a good match with FD solvers of CST and HFSS. Also, with the accuracy of -60 dB, the simulation time of 100 pulses and sufficient mesh, TD solver of CST provides us good solutions in a reasonable simulation time duration. For all simulations results presented in this paper are done using TD solver of CST.

For example, the co polarization simulated RCS signals for the front side of the proposed scatterer aligned at an angle $\theta = 0^\circ$ are denoted as $S_{\text{HH}}^{\text{F(CST)}}(0^\circ)$ and $S_{\text{VV}}^{\text{F(CST)}}(0^\circ)$. Here, the subscript corresponds to the polarization. The superscript corresponds to the side of the scatterer showing F or R for the front or rear side, respectively. The superscript mentions also that the RCS signals are estimated by the CST simulations. The argument shows the alignment angle θ . The alignment angles θ can be seen in the silkscreen of the realized circuit in Fig. 2(a).

Fig. 3 shows the co polarization backscattered simulated RCS signals $S_{\text{HH}}^{\text{F(CST)}}(0^\circ)$ and $S_{\text{VV}}^{\text{F(CST)}}(0^\circ)$ of the front side of the proposed scatterer aligned at $\theta = 0^\circ$. At $\theta = 0^\circ$, the dipoles of the proposed scatterer are aligned vertically. For this reason, $S_{\text{VV}}^{\text{F(CST)}}(0^\circ)$ presents the resonance dips [see the light blue dashed line in Fig. 3(inset)]. On the other hand, $S_{\text{HH}}^{\text{F(CST)}}(0^\circ)$ presents non-resonant signals [see the black solid line in Fig. 3(inset)]. These non-resonant signals are from the specular reflections from the circular shape. The cross polarization signals $S_{\text{HV}}^{\text{F(CST)}}(0^\circ)$ and $S_{\text{VH}}^{\text{F(CST)}}(0^\circ)$ are close to null because of the symmetrical shape of the scatterer.

At $\theta = 45^\circ$ facing the front side to polarimetric radar, the proposed scatterer becomes a depolarizing scatterer and backscatter all four components of the simulated scattering matrix $\mathbf{S}^{\text{F(CST)}}(45^\circ)$. The simulated co polarization RCS signals $S_{\text{HH}}^{\text{F(CST)}}(45^\circ)$ and $S_{\text{VV}}^{\text{F(CST)}}(45^\circ)$ are the amplitude reduced versions of the $S_{\text{VV}}^{\text{F(CST)}}(0^\circ)$. This reduction in amplitude occurs due to the angle $\theta = 45^\circ$ of dipoles with respect to the polarization of incident signal. Fig. 4 shows the cross polarization backscattered simulated RCS signals $S_{\text{HV}}^{\text{F(CST)}}(45^\circ)$ and $S_{\text{VH}}^{\text{F(CST)}}(45^\circ)$ along with their fit signals $S_{\text{HV}}^{\text{F(CST-fit)}}(45^\circ)$ and $S_{\text{VH}}^{\text{F(CST-fit)}}(45^\circ)$ of the front side of the proposed scatterer aligned at $\theta = 45^\circ$. The fitting of the signals is done by using a first degree polynomial. Here, the fit signals

are achieved based on the peak apexes associated with the dipoles present in the design of the proposed scatterer. The detection amplitude range for these peak apexes is chosen equal to 3 dB relative to the peak apex with maximum amplitude.

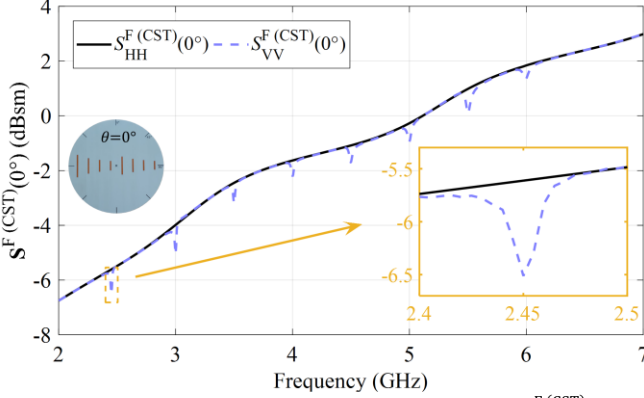


Fig. 3. Co polarization backscattered simulated RCS signals $S_{HH}^F(CST)(0^\circ)$ and $S_{VV}^F(CST)(0^\circ)$ of the front side of the proposed scatterer aligned at $\theta = 0^\circ$. Insets: zoom-in of the first resonance dip.

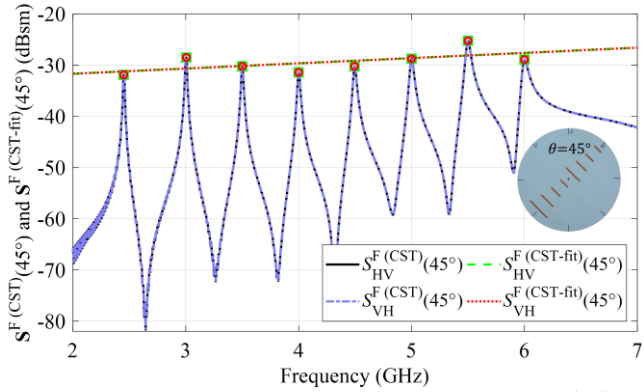


Fig. 4. Cross polarization backscattered simulated RCS signals $S_{HV}^F(CST)(45^\circ)$ and $S_{VH}^F(CST)(45^\circ)$ along with their fit signals $S_{HV}^F(CST-fit)(45^\circ)$ and $S_{VH}^F(CST-fit)(45^\circ)$ of the front side of the proposed scatterer aligned at $\theta = 45^\circ$. The symbols \circ and \square present the peak apexes of signals.

The rear side of the proposed scatterer [see Fig. 2(b)] behaves like a metallic disk. The copper thickness of the trace is $t = 35 \mu\text{m}$. Fig. 5 shows the co polarization backscattered simulated RCS signals $S_{HH}^R(CST)$ and $S_{VV}^R(CST)$ of the rear side of the proposed scatterer. Here, too, the cross polarization signals $S_{HV}^R(CST)$, and $S_{VH}^R(CST)$ are close to null because of the symmetrical shape of the scatterer.

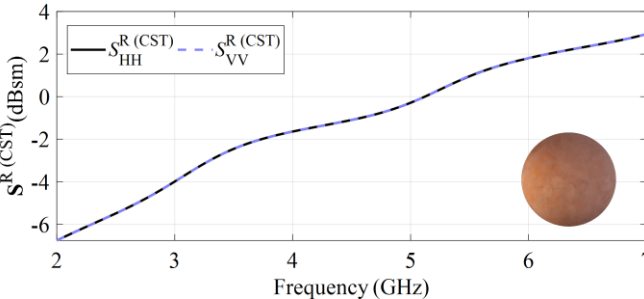


Fig. 5. Co polarization backscattered simulated RCS signals $S_{HH}^R(CST)$ and $S_{VV}^R(CST)$ of the rear side of the proposed scatterer.

B. Supplementary scatterers

Three supplementary scatterers are also realized. Fig. 6 shows the photographs of the metallic disk, the dihedral, and the depolarizing RF Elementary Particle (REP) chipless RFID tag. The metallic disk [Fig. 6(a)] and the dihedral tilted at 22.5° [Fig. 6(b)] will be used as standard calibration objects to make a reference calibration for the comparison with the calibration performed using the proposed scatterer. On the other hand, the dihedral tilted at 45° [Fig. 6(b)] as well as the REP chipless tag [Fig. 6(c)] will be used as the test targets for the radar calibration.

The metallic disk and the dihedral are realized using a copper sheet with metal thickness $t' = 100 \mu\text{m}$. The utilized copper sheet is with a brushed or polished finish as advised in [8]. The disk, the rear side of the proposed scatterer and the dihedral are the broadband scatterers. In general, the dimensions of these broadband scatterers are a few λ [17]. However, in our case, the dimensions of these scatterers are comparable to λ .

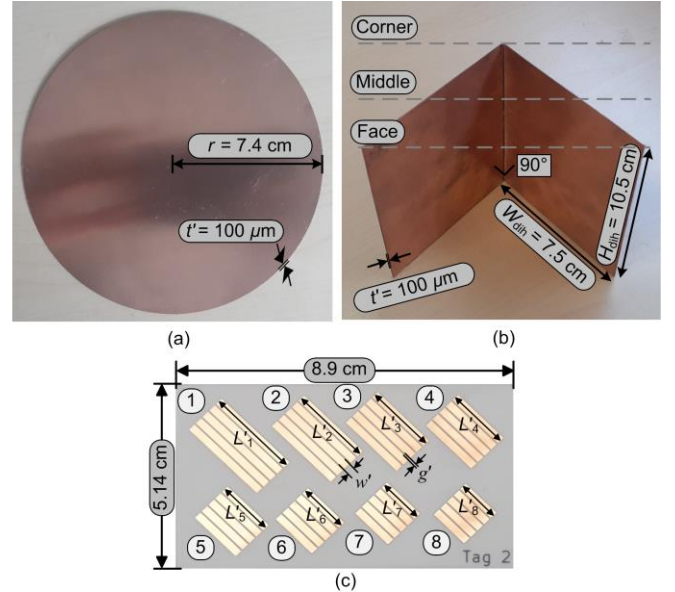


Fig. 6. Photographs of the supplementary scatterers. (a) Metallic disk. (b) Dihedral. (c) Depolarizing RF Elementary Particle (REP) chipless RFID tag [18].

The radius of the metallic disk [see Fig. 6(a)] is $r = 7.4 \text{ cm}$ that is chosen precisely the same as the proposed scatterer for comparison purposes. For normal incidence plane wave, the theoretical scattering matrix of perfectly conducting circular disk \mathbf{S}^{disk} is estimated as [19]:

$$\mathbf{S}^{\text{disk}} = \frac{4\pi A^2}{\lambda^2} \begin{bmatrix} 1 & 0 \\ 0 & 1 \end{bmatrix} \quad (4)$$

where $A = \pi r^2$ is the area of the metallic disk. Fig. 7 shows a comparison among the theoretical RCS of the metallic disk S_{VV}^{disk} calculated using (4), the CST estimated RCS of the metallic disk $S_{VV}^{\text{disk}(CST)}$, and the CST estimated RCS of the rear side of the proposed scatterer $S_{VV}^R(CST)$. It can be observed that $S_{VV}^R(CST)$ is in good agreement with S_{VV}^{disk} of (4) and $S_{VV}^{\text{disk}(CST)}$.

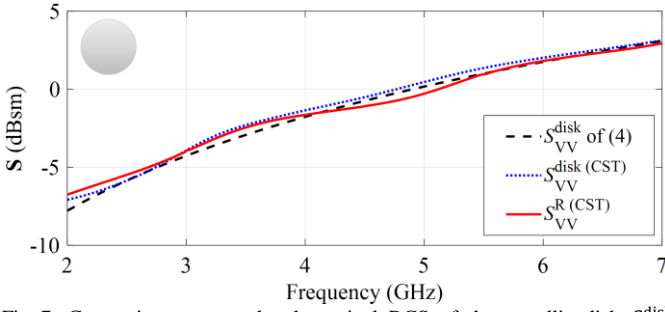


Fig. 7. Comparison among the theoretical RCS of the metallic disk S_{VV}^{disk} calculated using (4), the CST estimated RCS of the metallic disk $S_{VV}^{\text{disk (CST)}}$, and the CST estimated RCS of the rear side of the proposed scatterer $S_{VV}^{\text{R (CST)}}$.

The dihedral [see Fig. 6(b)] is constituted of two identical rectangular faces creased and folded at a right angle. The height and the width of the rectangular faces are $H_{\text{dih}}=10.5$ cm and $W_{\text{dih}}=7.5$ cm, respectively. For calculating the distance from the radar antenna to the dihedral three reference planes are considered: face, middle, and corner. These reference planes will be taken into account later in this paper.

With the normal incidence of plane wave, the maximum scattering coefficient $S^{\text{vert. dih.}}$ from a dihedral with corner parallel to the V polarization is [20]:

$$S^{\text{vert. dih.}} = 8\pi \left(\frac{W_{\text{dih}} H_{\text{dih}}}{\lambda} \right)^2. \quad (5)$$

The scattering matrix of a vertically aligned dihedral (i.e., at 0°) is estimated as [20]:

$$\mathbf{S}^{\text{dih.}}(0^\circ) = \sqrt{S^{\text{vert. dih.}}} \begin{bmatrix} -1 & 0 \\ 0 & 1 \end{bmatrix}. \quad (6)$$

Tilted dihedral behaves like a depolarizing scatterer:

$$\mathbf{S}^{\text{dih.}}(\theta') = \sqrt{S^{\text{vert. dih.}}} \begin{bmatrix} -\cos(2\theta') & \sin(2\theta') \\ \sin(2\theta') & \cos(2\theta') \end{bmatrix} \quad (7)$$

where θ' is the angle of inclination. It is important to note that the scattering matrix of the tilted dihedral (7) can be computed from the scattering matrix of the vertically oriented dihedral (6).

At $\theta' = 22.5^\circ$, (7) becomes

$$\mathbf{S}^{\text{dih.}}(22.5^\circ) = \frac{\sqrt{S^{\text{vert. dih.}}}}{2} \begin{bmatrix} -1 & 1 \\ 1 & 1 \end{bmatrix} \quad (8)$$

where the magnitude of all four components of the scattering matrix is equal. Therefore, a dihedral inclined at 22.5° produces strong cross polarization signals which are also linearly independent from the co polarization scatterers.

Fig. 8 presents a comparison of the theoretical cross polarization RCS signals $[S_{HV}^{\text{dih.}}(22.5^\circ)]$ and $[S_{VH}^{\text{dih.}}(22.5^\circ)]$ calculated using (8), and the CST estimated cross polarization RCS signals $[S_{HV}^{\text{dih. (CST)}}(22.5^\circ)]$ and $[S_{VH}^{\text{dih. (CST)}}(22.5^\circ)]$ for dihedral tilted at $\theta'=22.5^\circ$. The $S_{HV}^{\text{dih. (CST)}}(22.5^\circ)$ and $S_{VH}^{\text{dih. (CST)}}(22.5^\circ)$ present slight ripples because the dimensions of dihedral (H_{dih} and W_{dih}) are not very large as compared to λ . The maximum difference between the

amplitude of the theoretical RCS signals $[S_{HV}^{\text{dih.}}(22.5^\circ)]$ and $S_{VH}^{\text{dih.}}(22.5^\circ)$ calculated using (8) and CST estimated RCS signals $[S_{HV}^{\text{dih. (CST)}}(22.5^\circ)]$ and $S_{VH}^{\text{dih. (CST)}}(22.5^\circ)$ is 3.7 dB.

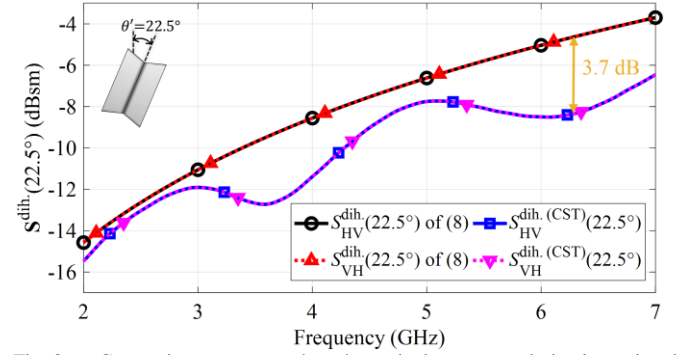


Fig. 8 Comparison among the theoretical cross polarization signals $S_{HV}^{\text{dih.}}(22.5^\circ)$ and $S_{VH}^{\text{dih.}}(22.5^\circ)$ calculated using (8), and the CST estimated cross polarization RCS signals $S_{HV}^{\text{dih. (CST)}}(22.5^\circ)$ and $S_{VH}^{\text{dih. (CST)}}(22.5^\circ)$ for dihedral tilted at $\theta'=22.5^\circ$.

The REP chipless tag [Fig. 6(c)] is composed of eight 45° shorted dipoles with frequencies of operation in UWB (see [18]). This tag is realized using PCB technology on a Rogers RO4003C substrate with substrate height $h = 0.81$ mm and dielectric permittivity $\epsilon_r = 3.55$. Each coupled dipole exhibits the microstrip trace width is $w' = 2$ mm and the metal thickness $t = 35$ μm . The space between multiple coupled dipoles is $g' = 0.5$ mm. The lengths of 45° shorted dipoles L'_i are $L'_1=24.8$ mm, $L'_2=21.8$ mm, $L'_3=19$ mm, $L'_4=16.8$ mm, $L'_5=15$ mm, $L'_6=13.4$ mm, $L'_7=12.2$ mm, $L'_8=11.2$ mm. The overall size dimensions are 8.9×5.14 cm^2 . These geometrical dimensions are provided to facilitate the reproduction for the reader. A detailed discussion on the bandwidths of the resonators and RCS levels can be seen in [12, Chap. 4].

For the sake of simplicity, Fig. 9 presents a co polarization $S_{VV}^{\text{tag (CST)}}$ component and a cross polarization $S_{HV}^{\text{tag (CST)}}$ component of the CST estimated scattering matrix $\mathbf{S}^{\text{tag (CST)}}$ for the REP chipless RFID tag. The gray regions show a 100 MHz range around all eight peak apexes of the REP chipless RFID tag.

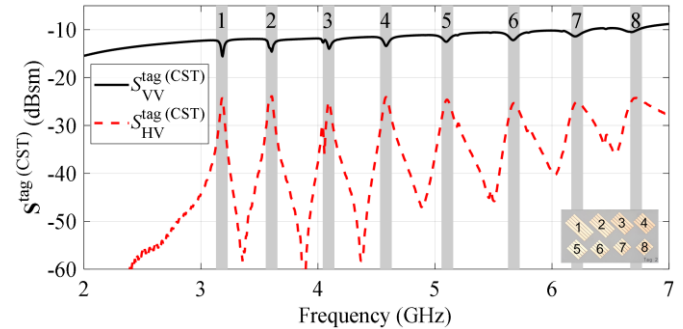


Fig. 9 CST estimated RCS signals $S_{VV}^{\text{tag (CST)}}$ and $S_{HV}^{\text{tag (CST)}}$ for the REP chipless RFID tag. The gray regions show a 100 MHz range around all eight peak apexes of the REP chipless RFID tag.

V. POLARIMETRIC RADAR CALIBRATION PROCEDURES

The full polarimetric radar calibration is performed using a single antenna based calibration technique found in the literature [4]. This technique is valid for the polarimetric radar

systems with good cross polarization isolation between the antenna ports (i.e., 30 dB in our case). Therefore, this technique suits well for the measurement radar system adopted in this paper (see Fig. 1). The calibration technique (for more details, see [4]) requires two calibration objects. The first calibration target is with dominant co polarized scattering behavior, while the second calibration target is with strong cross polarized scattering behavior. The exact scattering matrix for the second calibration target needs not to be known. Therefore, the calibration is primarily dependent on the nondepolarizing object (namely calibration Type 1). Similarly, the polarimetric radar calibration can also be made primarily dependent on the depolarizing object (namely calibration Type 2). In such a case, the first calibration target is with strong cross polarized scattering behavior, while the second calibration target is with dominant co polarized scattering behavior.

In this paper, we made this approach compatible with the use of resonant scatterer which is not done in [4].

A. Calibration Primarily Dependent on Nondepolarizing Object (Calibration Type 1)

For the co polarization calibration, the exact co polarization scattering of the first calibration target (i.e., with dominant co polarized scattering behavior) S_0 must be known. In our case, the object dimensions are smaller as compared to λ . For this reason, the simulation results from full-wave CST simulator are the best choice for the estimation of S_0 .

For measured signals, it is important to note the scattering matrix is similar to \mathbf{M} as expressed in (2). The measurements matrix of the first calibration target \mathbf{M}^0 need to be measured by placing the target at a distance d_0 . Then, for an unknown test target with the measurement matrix \mathbf{M}^u measured at a distance d_u , the calibrated co polarization components $C1_{VV}^u$ and $C1_{HH}^u$ of the calibrated scattering matrix of an unknown test object $\mathbf{C1}^u$ are estimated as [4]:

$$C1_{VV}^u = \left(\frac{M_{VV}^u}{M_{VV}^0} \right) \left(\frac{d_u}{d_0} \right)^2 e^{-i2k(d_0-d_u)} S_0 \quad (9)$$

$$C1_{HH}^u = \left(\frac{M_{HH}^u}{M_{HH}^0} \right) \left(\frac{d_u}{d_0} \right)^2 e^{-i2k(d_0-d_u)} S_0 \quad (10)$$

where k is the wavenumber. The superscript and subscript u refers to the unknown test object.

For the cross polarization calibration, the measurements matrix of the second calibration target \mathbf{M}^c (i.e., with strong cross polarized scattering behavior) need to be measured by placing the target at a distance d_c . Then, the calibrated cross polarization components $C1_{HV}^u$ and $C1_{VH}^u$ of $\mathbf{C1}^u$ of the unknown test object are estimated as [4]:

$$C1_{HV}^u = \frac{M_{HV}^u}{\sqrt{K_1 K_2}} \left(\frac{d_u}{d_0} \right)^2 e^{-i2k(d_0-d_u)} S_0 \quad (11)$$

$$C1_{VH}^u = \sqrt{\frac{K_1}{K_2}} M_{VH}^u \left(\frac{d_u}{d_0} \right)^2 e^{-i2k(d_0-d_u)} S_0 \quad (12)$$

where $K_1 = M_{HV}^c/M_{VH}^c$ and $K_2 = M_{VV}^0/M_{HH}^0$. It is important to note that the knowledge of the exact scattering matrix of the cross polarized scattering object is not required and only the measured cross polarized signals M_{HV}^c and M_{VH}^c are needed to compute K_1 . Using (9), (10), (11), and (12), the polarimetric radar calibration Type1 is done.

B. Calibration Primarily Dependent on Depolarizing Object (Calibration Type 2)

Here, the first calibration target is with strong cross polarized scattering behavior, while the second calibration target is with dominant co polarized scattering behavior. The exact cross polarization scattering of the first calibration target (i.e., with strong cross polarized scattering behavior) S_c must be known. Then, the calibrated cross polarization components $C2_{HV}^u$ and $C2_{VH}^u$ of the calibrated scattering matrix $\mathbf{C2}^u$ are estimated as:

$$C2_{HV}^u = \left(\frac{M_{HV}^u}{M_{HV}^c} \right) \left(\frac{d_u}{d_c} \right)^2 e^{-i2k(d_c-d_u)} S_c \quad (13)$$

$$C2_{VH}^u = \left(\frac{M_{VH}^u}{M_{VH}^c} \right) \left(\frac{d_u}{d_c} \right)^2 e^{-i2k(d_c-d_u)} S_c. \quad (14)$$

The calibrated co polarization components $C2_{VV}^u$ and $C2_{HH}^u$ of $\mathbf{C2}^u$ are estimated as:

$$C2_{VV}^u = \frac{M_{VV}^u}{\sqrt{K'_1 K'_2}} \left(\frac{d_u}{d_c} \right)^2 e^{-i2k(d_c-d_u)} S_c \quad (15)$$

$$C2_{HH}^u = \sqrt{\frac{K'_1}{K'_2}} M_{HH}^u \left(\frac{d_u}{d_c} \right)^2 e^{-i2k(d_c-d_u)} S_c \quad (16)$$

where $K'_1 = M_{VV}^0/M_{HH}^0$ and $K'_2 = M_{HV}^c/M_{VH}^c$. Using (13), (14), (15), and (16), the polarimetric radar calibration Type 2 is done.

VI. RADAR CALIBRATION RESULTS

First, the radar calibration is performed using well-known standard calibration objects: the metallic disk [Fig. 6(a)] and the dihedral tilted at 22.5° [Fig. 6(b)]. Then, the radar calibration is done using the proposed scatterer. The performance of both calibration target sets is compared. For this purpose, two test targets are utilized: the dihedral tilted at 45° [Fig. 6(b)] and the REP chipless tag [Fig. 6(c)].

A. Radar Calibration Results Using Metallic Disk and Dihedral Tilted at 22.5°

For the standard calibration, we used the metallic disk (i.e., with dominant co polarized scattering behavior) [see Fig. 6(a)] and the dihedral tilted at 22.5° (i.e., with strong cross polarized scattering behavior) [see Fig. 6(b)]. The co polarization signals of the metallic disk M_{HH}^{disk} and M_{VV}^{disk} are measured at distance $d_0 = 28$ cm. Then, the cross polarization signals of the dihedral tilted at 22.5° $M_{HV}^{\text{dih.}(22.5^\circ)}$ and $M_{VH}^{\text{dih.}(22.5^\circ)}$ are measured. The distance from the radar

antenna and the dihedral tilted at 22.5° is calculated with respect to face [see Fig. 6(b)] as a reference plane, that is, $d_c^f = 28$ cm. So, $d_c = d_c^f$. The description of utilized signals for Type 1 and Type 2 calibrations are provided in Table II.

TABLE II
THE UTILIZED SIGNALS FOR TYPE 1 AND TYPE 2 CALIBRATIONS USING METALLIC DISK AND DIHEDRAL TILTED AT 22.5° .

Type of Calibration	Signals
Calibration	$S_0 = S_{VV}^{\text{disk (CST)}}$
Type 1	$M_{HH}^0 = M_{HH}^{\text{disk}}$ and $M_{VV}^0 = M_{VV}^{\text{disk}}$
(9) to (12)	$M_{HV}^c = M_{HV}^{\text{dih.}(22.5^\circ)}$ and $M_{VH}^c = M_{VH}^{\text{dih.}(22.5^\circ)}$
Calibration	$S_c = S_{HV}^{\text{dih. (CST)}(22.5^\circ)}$
Type 2	$M_{HH}^0 = M_{HH}^{\text{disk}}$ and $M_{VV}^0 = M_{VV}^{\text{disk}}$
(13) to (16)	$M_{HV}^c = M_{HV}^{\text{dih.}(22.5^\circ)}$ and $M_{VH}^c = M_{VH}^{\text{dih.}(22.5^\circ)}$

The first test object is the dihedral tilted at 45° . At $\theta' = 45^\circ$, the scattering matrix of the dihedral (7) becomes:

$$\mathbf{S}^{\text{dih.}(45^\circ)} = \sqrt{S^{\text{vert. dih.}}} \begin{bmatrix} 0 & 1 \\ 1 & 0 \end{bmatrix}. \quad (17)$$

Therefore, the dihedral tilted at 45° is a full depolarizing scattering object. For a dihedral tilted at 45° , the cross polarization CST estimated RCS signals are $S_{HV}^{\text{dih. (CST)}(45^\circ)}$ and $S_{VH}^{\text{dih. (CST)}(45^\circ)}$ and the measured cross polarization signals are $M_{HV}^{\text{dih.}(45^\circ)}$ and $M_{VH}^{\text{dih.}(45^\circ)}$. The radar calibrations Type 1 and Type 2 are done using $M_{HV}^u = M_{HV}^{\text{dih.}(45^\circ)}$ and $M_{VH}^u = M_{VH}^{\text{dih.}(45^\circ)}$ with $d_u = 28$ cm used in from (9) to (16). It is important to note that the dihedral tilted at 45° (i.e., a test object) is measured always with respect to the face [see Fig. 6(b)] as a reference plane.

Fig. 10 presents the calibrated RCS signals $C1_{HV}^{\text{dih.}(45^\circ)}$ and $C1_{VH}^{\text{dih.}(45^\circ)}$ in comparison to the CST estimated signal $S_{HV}^{\text{dih. (CST)}(45^\circ)}$. The calibration error signals are calculated such that $\Delta S1_{HV}^{\text{dih.}(45^\circ)} = C1_{HV}^{\text{dih.}(45^\circ)} - S_{HV}^{\text{dih. (CST)}(45^\circ)}$ and $\Delta S2_{HV}^{\text{dih.}(45^\circ)} = C2_{HV}^{\text{dih.}(45^\circ)} - S_{HV}^{\text{dih. (CST)}(45^\circ)}$. For intuition, the calibration error signals $\Delta S1_{HV}^{\text{dih.}(45^\circ)}$, $\Delta S1_{VH}^{\text{dih.}(45^\circ)}$, $\Delta S2_{HV}^{\text{dih.}(45^\circ)}$, and $\Delta S2_{VH}^{\text{dih.}(45^\circ)}$ are presented in Fig. 11. For the calibration Type 1 error signals $\Delta S1_{HV}^{\text{dih.}(45^\circ)}$ and $\Delta S1_{VH}^{\text{dih.}(45^\circ)}$, the maximum absolute calibration error $|\Delta S1_{\text{dih.}}^{\text{max}}|$ is 3.81 dB for the frequency range from 2 to 7 GHz, whereas, $|\Delta S1_{\text{dih.}}^{\text{max}}|$ is 2.36 dB for the frequency range from 2 to 6 GHz. On the other hand, for the calibration Type 2 error signals $\Delta S2_{HV}^{\text{dih.}(45^\circ)}$ and $\Delta S2_{VH}^{\text{dih.}(45^\circ)}$, the maximum absolute calibration error $|\Delta S2_{\text{dih.}}^{\text{max}}|$ is 0.65 dB for the frequency range from 2 to 7 GHz. The calibration Type 2 presents better accuracy as compared to the calibration Type 1 for the dihedral tilted at 45° as the test target. One reason for the low accuracy of calibration Type 1 is that the measured signals of the metallic disk M_{HH}^{disk} and M_{VV}^{disk} are not as smooth as the measured signals of the dihedral tilted at 22.5° $M_{HV}^{\text{dih.}(22.5^\circ)}$ and $M_{VH}^{\text{dih.}(22.5^\circ)}$ because the metallic disk is very sensitive to its center alignment. This sensitivity is discussed later in this paper. Also, the size of the metallic disk is not very large as

compared d to λ .

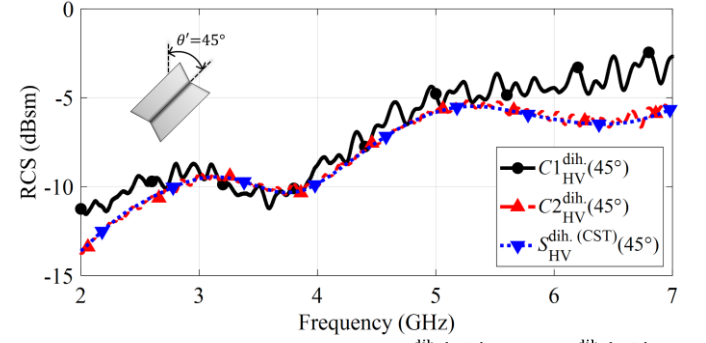


Fig. 10 The calibrated RCS signals $C1_{HV}^{\text{dih.}(45^\circ)}$ and $C2_{HV}^{\text{dih.}(45^\circ)}$ in comparison to the CST estimated signal $S_{HV}^{\text{dih. (CST)}(45^\circ)}$ for the dihedral tilted at 45° as the test target.

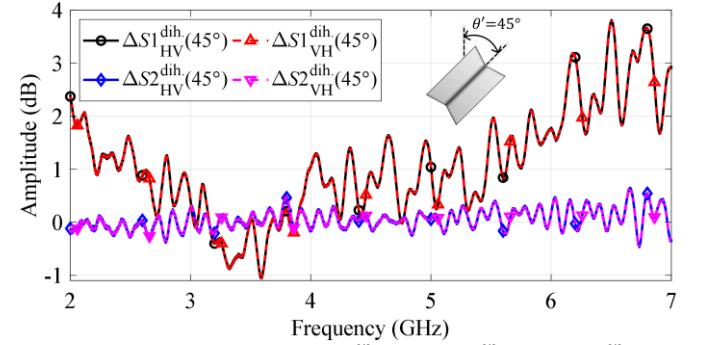


Fig. 11. Calibration error signals $\Delta S1_{HV}^{\text{dih.}(45^\circ)}$, $\Delta S1_{VH}^{\text{dih.}(45^\circ)}$, $\Delta S2_{HV}^{\text{dih.}(45^\circ)}$, and $\Delta S2_{VH}^{\text{dih.}(45^\circ)}$ for the dihedral tilted at 45° as the test target.

The measurement setup of monostatic radar used in this paper is in a vertical configuration to prove the concept. Other configurations of the radar (e.g., horizontal or tilted configurations) are also practically applicable. With such non-vertical measurement configurations and the mounting of scattering objects from their rear side, a major limiting factor of the dihedral as the calibration object is its large height. In such cases, the height of the dihedral should be compensated to keep a fixed distance. The accuracy of calibration Type 1 is not mainly affected due to the compensation error of height of dihedral as the calibration Type 1 is primarily dependent on the nondepolarizing object [see (9) to (12)]. However, the calibration Type 2 is primarily dependent on the depolarizing object [see (13) to (16)], so its accuracy is also dependent on the compensation error of height of dihedral. Fig. 12 presents the calibration error signals $\Delta S2_{HV}^{\text{dih.}(45^\circ)}$, where the distance between the radar antenna and the dihedral tilted at 22.5° is calculated with respect to: the face $d_c^f = 28$ cm, the middle $d_c^m = 28$ cm and the corner $d_c^c = 28$ cm. The maximum absolute calibration errors are $|\Delta S2_{\text{dih.}(a_c^f)}^{\text{max}}| = 0.65$ dB at d_c^f (same as the diamond and down-ward pointing triangle marked lines in Fig. 11), $|\Delta S2_{\text{dih.}(a_c^m)}^{\text{max}}| = 2.23$ dB at d_c^m , and $|\Delta S2_{\text{dih.}(a_c^c)}^{\text{max}}| = 3.07$ dB at d_c^c .

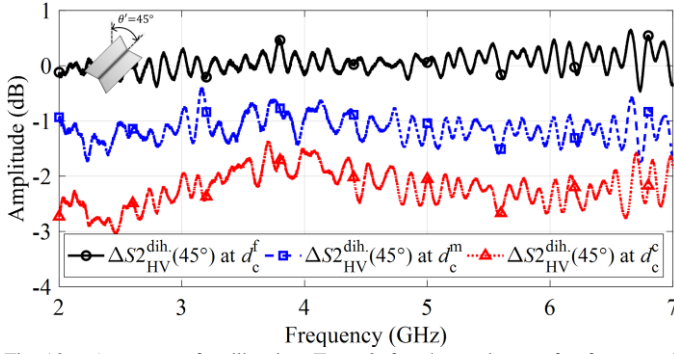


Fig. 12. Accuracy of calibration Type 2 for three planes of reference of dihedral tilted at 22.5°. The dihedral tilted at 45° is used as the test target.

The second test object is the REP chipless RFID tag. Here, the radar calibrations Type 1 and Type 2 are done using $\mathbf{M}^u = \mathbf{M}^{\text{tag}}$ with $d_u = 28$ cm used in from (9) to (16). The co polarization calibrated RCS signals $C1_{VV}^{\text{tag}}$ and $C2_{VV}^{\text{tag}}$ in comparison to the CST estimated RCS signal $S_{VV}^{\text{tag}(CST)}$ are presented in Fig. 13(a) and the cross polarization calibrated RCS signals $C1_{HV}^{\text{tag}}$ and $C2_{HV}^{\text{tag}}$ in comparison to the CST estimated RCS signal $S_{HV}^{\text{tag}(CST)}$ are presented in Fig. 13(b). A good agreement between the RCS components of \mathbf{C}^{tag} and $\mathbf{S}^{\text{tag}(CST)}$ is observed. Note that the errors should be observed within the gray regions. The reason behind this is due to the resonant behavior of REP chipless RFID tag, only the gray highlighted frequency ranges exhibit the acceptable level of SNR. Otherwise of these ranges, the backscattered SNR is too low. Fig. 14 presents calibration error signals $\mathbf{S1}^{\text{tag}}$ and $\mathbf{S2}^{\text{tag}}$ for the frequency range from 2 to 7 GHz. The co polarization calibration error signals [see Fig. 14(a)] are calculated such that $\Delta S1_{VV \text{ or } HH}^{\text{tag}} = C1_{VV \text{ or } HH}^{\text{tag}} - S_{VV \text{ or } HH}^{\text{tag}(CST)}$ and $\Delta S2_{VV \text{ or } HH}^{\text{tag}} = C2_{VV \text{ or } HH}^{\text{tag}} - S_{VV \text{ or } HH}^{\text{tag}(CST)}$. For the cross polarization [see Fig. 14(b)], first, the peak apexes of the RCS signals are detected $C1_{HV \text{ or } HV}^{\text{tag}'}$, $C2_{HV \text{ or } HV}^{\text{tag}'}$, $S_{HV \text{ or } HV}^{\text{tag}'(CST)}$ and then the calibration error signals are calculated such that $\Delta S1_{HV \text{ or } HV}^{\text{tag}} = C1_{HV \text{ or } HV}^{\text{tag}'}$ - $S_{HV \text{ or } HV}^{\text{tag}'(CST)}$ and $\Delta S2_{HV \text{ or } HV}^{\text{tag}} = C2_{HV \text{ or } HV}^{\text{tag}'}$ - $S_{HV \text{ or } HV}^{\text{tag}'(CST)}$. Such peak-to-peak calibration errors are calculated to present the results clearly. Otherwise, the observation of errors seems to be very difficult for the reader.

The co polarization error signals of calibration Type 1 $\Delta S1_{VV}^{\text{tag}}$ present the maximum absolute calibration error $|\Delta S1_{\text{tag}(VV)}^{\text{max}}|$ around 3 dB and $\Delta S1_{HH}^{\text{tag}}$ the maximum absolute calibration error $|\Delta S1_{\text{tag}(HH)}^{\text{max}}|$ around 3.28 dB for the frequency range from 2 to 7 GHz. Whereas, for co polarization error signals of the calibration Type 2 $\Delta S2_{VV}^{\text{tag}}$ exhibit the maximum absolute calibration error $|\Delta S2_{\text{tag}(VV)}^{\text{max}}| = 1.6$ dB and $\Delta S2_{HH}^{\text{tag}}$ exhibit the maximum absolute calibration error $|\Delta S2_{\text{tag}(HH)}^{\text{max}}| = 2.56$ dB.

The cross polarization error signals of calibration Type 1 $\Delta S1_{HV}^{\text{tag}}$ the maximum absolute calibration error $|\Delta S1_{\text{tag}(HV)}^{\text{max}}|$ around 2.36 dB and $\Delta S1_{VH}^{\text{tag}}$ present the maximum absolute

calibration errors $|\Delta S1_{\text{tag}(VH)}^{\text{max}}|$ around 2.33 dB for the frequency range from 2 to 7 GHz. On the other hand, the cross polarization error signals of calibration Type 2 $\Delta S2_{HV}^{\text{tag}}$ have the maximum absolute calibration error $|\Delta S2_{\text{tag}(HV)}^{\text{max}}|$ around 1.7 dB and $\Delta S2_{VH}^{\text{tag}}$ have the maximum absolute calibration error $|\Delta S2_{\text{tag}(VH)}^{\text{max}}|$ around 1.77 dB for the frequency range from 2 to 7 GHz. Therefore, the calibration Type 2 outperforms the calibration Type 1 as $\Delta S2^{\text{tag}} < \Delta S1^{\text{tag}}$ for the REP chipless RFID tag as the test target.

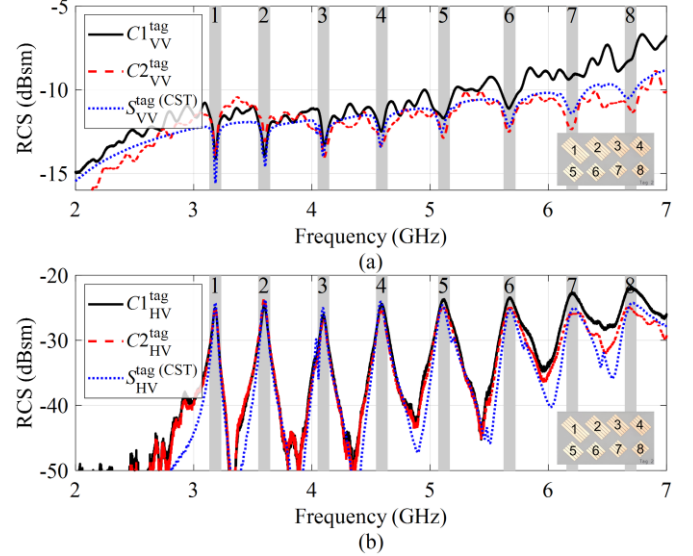


Fig. 13. The calibrated RCS signals $C1^{\text{tag}}$ and $C2^{\text{tag}}$ in comparison to the CST estimated signals $S^{\text{tag}(CST)}$ for the REP chipless RFID tag as the test target. (a) Co polarization RCS signals. (b) Cross polarization RCS signals. The gray regions show a 100 MHz range around all eight peak apexes of the REP chipless RFID tag.

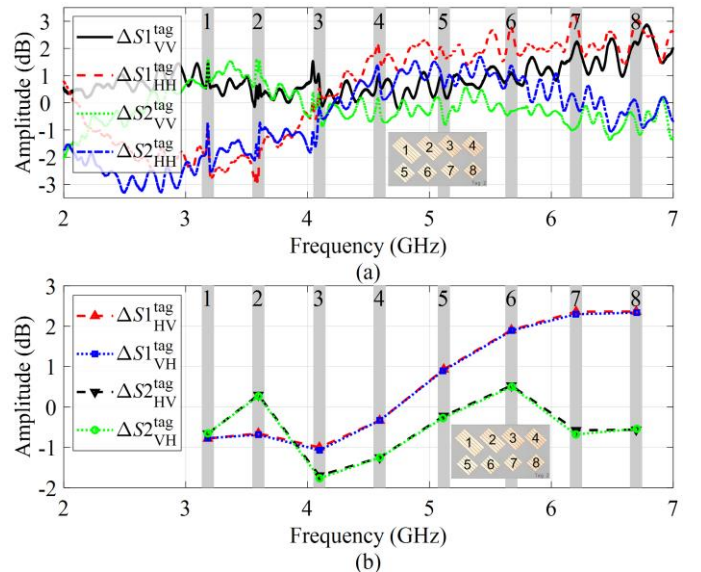


Fig. 14. Calibration error signals $\Delta S1^{\text{tag}}$ and $\Delta S2^{\text{tag}}$ for the REP chipless RFID tag as the test target. (a) Co polarization signals. (b) Cross polarization signals. The gray regions show a 100 MHz range around all eight peak apexes of the REP chipless RFID tag.

Fig. 15 presents the calibration error signals $\Delta S_{HH}^{\text{dih}}$ and $\Delta S_{HV}^{\text{dih}}$ for the three reference planes of dihedral tilted at 22.5°.

For details of the calculation, see the discussion of Fig. 12. The maximum absolute calibration errors shifts are from $|\Delta S_{\text{tag(HH), } d_c^f}^{\text{max}}| = 2.56$ dB. at d_c^f [same as the dashed-dotted line in Fig. 14(a)] to $|\Delta S_{\text{tag(HH), } d_c^c}^{\text{max}}| = 4.52$ dB at d_c^c and from $|\Delta S_{\text{tag(HV), } d_c^f}^{\text{max}}| = 1.76$ dB. at d_c^f [same as the downward pointing triangle marked line in Fig. 14(b)], to $|\Delta S_{\text{tag(HH), } d_c^c}^{\text{max}}| = 3.52$ dB at d_c^c .

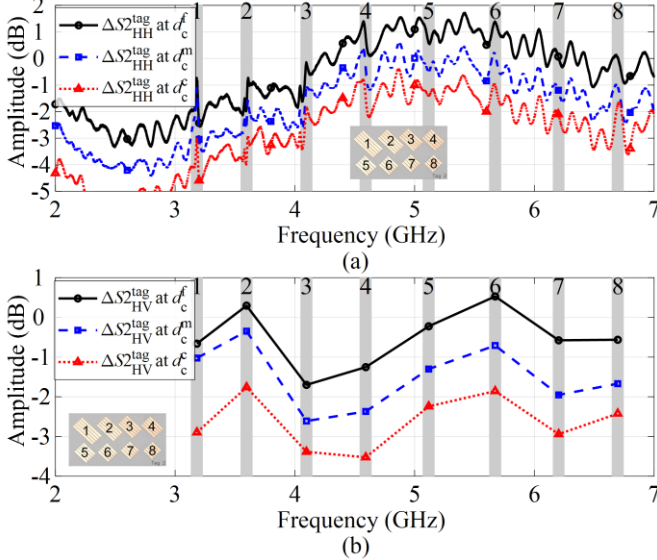


Fig. 15. Accuracy of calibration Type 2 for three planes of reference of dihedral tilted at 22.5° . The REP chipless RFID tag as the test target

B. Radar Calibration Results Using the Proposed Scatterer

For the radar calibration using the proposed scatterer, we used the rear side (i.e., provides dominant co polarized signals) [see Fig. 2(b)] and the front side tilted at 45° (i.e., provides strong cross polarized signals) [see Fig. 2(a)]. The co polarization signals of rear side of the proposed scatterer M_{HH}^{R} and M_{VV}^{R} are measured at distance $d_0 = 28$ cm. The cross polarization signals of front side of the proposed scatterer aligned at $\theta = 45^\circ$ $M_{\text{HV}}^{\text{F(fit)}}(45^\circ)$ and $M_{\text{VH}}^{\text{F(fit)}}(45^\circ)$ are measured at distance $d_c = 28$ cm. It is important to note that $M_{\text{HV}}^{\text{F(fit)}}(45^\circ)$ and $M_{\text{VH}}^{\text{F(fit)}}(45^\circ)$ are fit signals (similar to simulated signals presented in Fig. 4). The utilized signals for Type 1 and Type 2 calibrations are summarized in Table III.

TABLE III
THE UTILIZED SIGNALS FOR TYPE 1 AND TYPE 2 CALIBRATIONS USING THE PROPOSED SCATTERER.

Type of Calibration	Signals
Calibration	$S_0 = S_{\text{VV}}^{\text{R(CST)}}$
Type 1	$M_{\text{HH}}^0 = M_{\text{HH}}^{\text{R}}$ and $M_{\text{VV}}^0 = M_{\text{VV}}^{\text{R}}$
(9) to (12)	$M_{\text{HV}}^c = M_{\text{HV}}^{\text{F(fit)}}(45^\circ)$ and $M_{\text{VH}}^c = M_{\text{VH}}^{\text{F(fit)}}(45^\circ)$
Calibration	$S_c = S_{\text{HV}}^{\text{F(CST-fit)}}(45^\circ)$
Type 2	$M_{\text{HH}}^0 = M_{\text{HH}}^{\text{R}}$ and $M_{\text{VV}}^0 = M_{\text{VV}}^{\text{R}}$
(13) to (16)	$M_{\text{HV}}^c = M_{\text{HV}}^{\text{F(fit)}}(45^\circ)$ and $M_{\text{VH}}^c = M_{\text{VH}}^{\text{F(fit)}}(45^\circ)$

In this case, the same two test objects (the dihedral tilted at 45° and the REP chipless tag) measured at $d_u = 28$ cm are used. The radar calibrations Type 1 and Type 2 are done as

explained in Section V-A and B. To differentiate from the standard calibration results (from Section VI-A), the calibrated scattering matrices are used as primed $\mathbf{C1}'^u$ and $\mathbf{C2}'^u$ for the calibration results of the proposed scatterer.

For the dihedral tilted at 45° (i.e., used as the first test object), Fig. 16 presents the calibration error signals calculated as $\Delta \mathbf{S1}'^{\text{dih.}}(45^\circ) = \mathbf{C1}'^{\text{dih.}}(45^\circ) - \mathbf{S}^{\text{dih. (CST)}}(45^\circ)$ and $\Delta \mathbf{S2}'^{\text{dih.}}(45^\circ) = \mathbf{C2}'^{\text{dih.}}(45^\circ) - \mathbf{S}^{\text{dih. (CST)}}(45^\circ)$. For the calibration Type 1 error signals $\Delta \mathbf{S1}'^{\text{dih.}}(45^\circ)$ and $\Delta \mathbf{S1}^{\text{dih.}}(45^\circ)$, the maximum absolute calibration error $|\Delta \mathbf{S1}'^{\text{dih. max}}|$ is 3.76 dB, whereas, for the calibration Type 2 error signals $\Delta \mathbf{S2}'^{\text{dih.}}(45^\circ)$ and $\Delta \mathbf{S2}^{\text{dih.}}(45^\circ)$, the maximum absolute calibration error $|\Delta \mathbf{S2}'^{\text{dih. max}}|$ is 2.96 dB for the frequency range from 2 to 7 GHz. It is important to note that the proposed scatterer presents comparable performance to the standard calibration objects (the metallic disk and the dihedral tilted at 22.5°), where $|\Delta \mathbf{S1}'^{\text{dih. max}}|$ is slightly less than $|\Delta \mathbf{S1}^{\text{dih. max}}|$ and $|\Delta \mathbf{S2}'^{\text{dih. max}}|$ is comparable to $|\Delta \mathbf{S2}^{\text{dih. max}}(d_c^c)|$.

On the other hand, the calibrated scattering matrices obtained using the standard objects (the metallic disk and the dihedral tilted at 22.5°) $\mathbf{C1}^{\text{dih}}$ and $\mathbf{C2}^{\text{dih}}$ in Section VI-A might also be taken as the reference signals instead of the CST estimated RCS scattering matrix $\mathbf{S}^{\text{dih. (CST)}}$. In such a case, the calibration error matrix signals are calculated as $\Delta \mathbf{S1}''^{\text{dih.}} = \mathbf{C1}'^{\text{dih.}} - \mathbf{C1}^{\text{dih.}}$ and $\Delta \mathbf{S2}''^{\text{dih.}} = \mathbf{C2}'^{\text{dih.}} - \mathbf{C2}^{\text{dih.}}$. Fig. 17 presents the calibration error signals for calibrations Type 1 and 2. Here, the maximum absolute calibration errors $|\Delta \mathbf{S1}''^{\text{dih. max}}|$ is less than 1 dB for $\Delta \mathbf{S1}''^{\text{dih.}}$ and $|\Delta \mathbf{S2}''^{\text{dih. max}}|$ is around 2.96 dB for $\Delta \mathbf{S2}''^{\text{dih.}}$ for the frequency range from 2 to 7 GHz. The reason behind the large value of $|\Delta \mathbf{S2}''^{\text{dih. max}}|$ is that the cross polarization signals of front side of the proposed scatterer aligned at $\theta = 45^\circ$ $M_{\text{HV}}^{\text{F(fit)}}(45^\circ)$ and $M_{\text{VH}}^{\text{F(fit)}}(45^\circ)$ are not as strong as the cross polarization signals of the dihedral tilted at 22.5° $M_{\text{HV}}^{\text{dih.}}(22.5^\circ)$ and $M_{\text{VH}}^{\text{dih.}}(22.5^\circ)$.

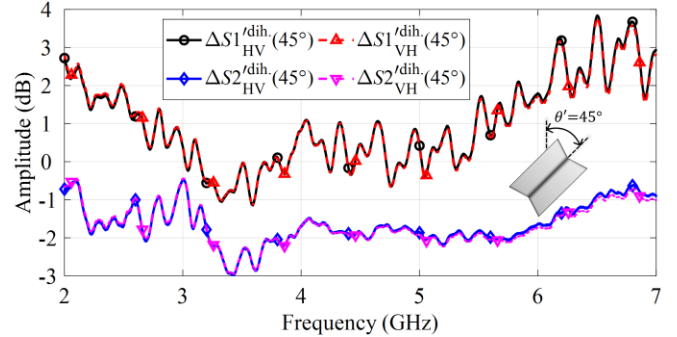


Fig. 16. Calibration error signals $\Delta \mathbf{S1}_{\text{HV}}^{\text{dih.}}(45^\circ)$, $\Delta \mathbf{S1}_{\text{VH}}^{\text{dih.}}(45^\circ)$, $\Delta \mathbf{S2}_{\text{HV}}^{\text{dih.}}(45^\circ)$ and $\Delta \mathbf{S2}_{\text{VH}}^{\text{dih.}}(45^\circ)$ for the dihedral tilted at 45° as the test target.

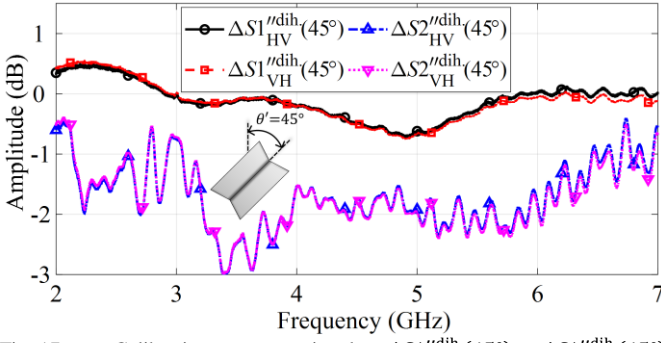


Fig. 17 Calibration error signals $\Delta S1_{HV}^{dih}(45^\circ)$, $\Delta S1_{VH}^{dih}(45^\circ)$, $\Delta S2_{HV}^{dih}(45^\circ)$ and $\Delta S2_{VH}^{dih}(45^\circ)$ for the dihedral tilted at 45° as the test target.

For the REP chipless RFID tag (i.e., used as the second calibration object), the calibrations are done and $C1^{tag}$ and $C2^{tag}$ are calculated. Fig. 18 presents the calibration error matrix signals $\Delta S1^{tag}$ and $\Delta S2^{tag}$ for the frequency range from 2 to 7 GHz. For details of the calculation of $\Delta S1^{tag}$ and $\Delta S2^{tag}$, see the discussion of Fig. 14, where the $C1^{tag}$ and $C2^{tag}$ should be replaced with $C1^{tag}$ and $C2^{tag}$. Note that the errors should be observed within gray regions.

The co polarization error signals of calibration Type 1 $\Delta S1_{VV}^{tag}$ present the maximum absolute calibration error $|\Delta S1_{tag(VV)}^{max}|$ around 2.33 dB and $\Delta S1_{HH}^{tag}$ the maximum absolute calibration error $|\Delta S1_{tag(HH)}^{max}|$ around 2.4 dB for the frequency range from 2 to 7 GHz. Whereas, for co polarization error signals of the calibration Type 2 $\Delta S2_{VV}^{tag}$ exhibit the maximum absolute calibration error $|\Delta S2_{tag(VV)}^{max}| = 2.76$ dB and $\Delta S2_{HH}^{tag}$ exhibit the maximum absolute calibration error $|\Delta S2_{tag(HH)}^{max}| = 4.68$ dB.

The cross polarization error signals of calibration Type 1 $\Delta S1_{HV}^{tag}$ the maximum absolute calibration error $|\Delta S1_{tag(HV)}^{max}|$ around 2.45 dB and $\Delta S1_{VH}^{tag}$ present the maximum absolute calibration errors $|\Delta S1_{tag(VH)}^{max}|$ around 2.29 dB for the frequency range from 2 to 7 GHz. On the other hand, the cross polarization error signals of calibration Type 2 $\Delta S2_{HV}^{tag}$ have the maximum absolute calibration error $|\Delta S2_{tag(HV)}^{max}|$ around 3.38 dB and $\Delta S2_{VH}^{tag}$ have the maximum absolute calibration error $|\Delta S2_{tag(VH)}^{max}|$ around 3.44 dB for the frequency range from 2 to 7 GHz. Here, the calibration Type 1 outperforms the calibration Type 2 as $\Delta S1^{tag} < \Delta S2^{tag}$ for the REP chipless RFID tag as the test target.

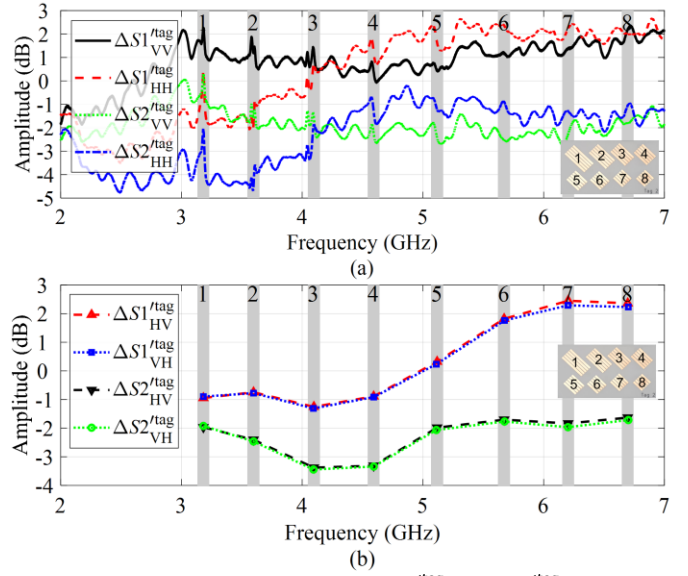


Fig. 18. Calibration error matrix signals $\Delta S1^{tag}$ and $\Delta S2^{tag}$ for the REP chipless RFID tag as the test target. (a) Co polarization signals. (b) Cross polarization signals. The gray regions show a 100 MHz range around all eight peak apexes of the REP chipless RFID tag.

The performance comparison between the proposed scatterer and the standard calibration objects (metallic disk and the dihedral tilted at 22.5°) for the REP chipless RFID tag as the test target is outlined in Table IV. For calibration Type 1, the performance of proposed scatterer is comparable to the standard calibration objects. For calibration Type 2, the performance of the standard calibration objects is better than the proposed scatterer. However, if the calibration errors for the three reference planes of dihedral tilted at 22.5° (see Fig. 15) are considered the performance of proposed scatterer is comparable to the standard calibration objects.

TABLE IV
PERFORMANCE COMPARISON BETWEEN THE PROPOSED SCATTERER AND THE STANDARD CALIBRATION OBJECTS FOR THE REP CHIPLESS RFID TAG AS THE TEST TARGET.

Type of Calibration	Proposed Scatterer	Standard Calibration Objects
Calibration Type 1	$ \Delta S1_{tag(VV)}^{max} = 2.33$ dB	$ \Delta S1_{tag(VV)}^{max} = 3$ dB
	$ \Delta S1_{tag(HH)}^{max} = 2.4$ dB	$ \Delta S1_{tag(HH)}^{max} = 3.28$ dB
	$ \Delta S1_{tag(HV)}^{max} = 2.45$ dB	$ \Delta S1_{tag(HV)}^{max} = 2.36$ dB
	$ \Delta S1_{tag(VH)}^{max} = 2.29$ dB	$ \Delta S1_{tag(VH)}^{max} = 2.33$ dB
Calibration Type 2	$ \Delta S2_{tag(VV)}^{max} = 2.76$ dB	$ \Delta S2_{tag(VV)}^{max} = 1.6$ dB
	$ \Delta S2_{tag(HH)}^{max} = 4.68$ dB	$ \Delta S2_{tag(HH)}^{max} = 2.56$ dB
	$ \Delta S2_{tag(HV)}^{max} = 3.38$ dB	$ \Delta S2_{tag(HV)}^{max} = 1.7$ dB
	$ \Delta S2_{tag(VH)}^{max} = 3.44$ dB	$ \Delta S2_{tag(VH)}^{max} = 1.77$ dB

One can argue that it would be more accurate to calculate calibration signals and the calibration errors using the radiative near field (Fresnel region) RCS simulated signals instead of the farfield simulated signals (see Table III and Fig. 18). We have done CST simulations of the proposed scatterer and the REP chipless RFID tag, where a plane wave is used for the excitation (the incident E field) and the E field probe at distance equals 28 cm (same as used in measurements) is used to compute the backscattered E field.

Then, the quasi RCS signals are calculated at distance of 28 cm. The calibration signals and calibration error signals are calculated, where all ideal RCS signals are the quasi RCS signals (not farfield RCS signals as done in Table III and Fig. 18). In such a case, we have observed that the calibration errors are larger as compared to calibration errors presented in Fig. 18. It is found that the farfield RCS signals provide better accuracy than the Fresnel zone RCS signals.

The calibration errors of the proposed scatterer are also calculated using $\mathbf{C1}^{\text{tag}}$ and $\mathbf{C2}^{\text{tag}}$ (obtained in Section VI-A) as reference signals instead of $\mathbf{S}^{\text{tag(CST)}}$. Fig. 19 presents the calibration error signals $\Delta\mathbf{S1}^{\prime\prime\text{tag}}$ and $\Delta\mathbf{S2}^{\prime\prime\text{tag}}$ for the REP chipless RFID tag as the test target for the frequency range from 2 to 7 GHz. These calibration error matrix signals are calculated as $\Delta\mathbf{S1}^{\prime\prime\text{tag}} = \mathbf{C1}^{\prime\prime\text{tag}} - \mathbf{C1}^{\text{tag}}$ and $\Delta\mathbf{S2}^{\prime\prime\text{tag}} = \mathbf{C2}^{\prime\prime\text{tag}} - \mathbf{C2}^{\text{tag}}$. The co polarization calibration errors of calibration Type 1 $\Delta\mathbf{S1}_{\text{VV}}^{\prime\prime\text{tag}}$ and $\Delta\mathbf{S1}_{\text{HH}}^{\prime\prime\text{tag}}$ are in the range of ± 1.3 dB. The cross polarization calibration errors of calibration Type 1 $\Delta\mathbf{S1}_{\text{HV}}^{\prime\prime\text{tag}}$ and $\Delta\mathbf{S1}_{\text{VH}}^{\prime\prime\text{tag}}$ are in the range from -0.6 to 0.1 dB. These values of $\Delta\mathbf{S1}^{\prime\prime\text{tag}}$ are significantly less than $\Delta\mathbf{S1}^{\text{tag}}$ (presented in Fig. 18). Therefore, the calculation of calibration errors using the Fresnel zone calibrated signals of chipless RFID tag $\mathbf{C1}^{\text{tag}}$ and $\mathbf{C2}^{\text{tag}}$ (from standard calibration set) is practical than the farfield simulated signals $\mathbf{S}^{\text{tag(CST)}}$ of chipless RFID tag. On the other hand, the calibration errors of calibration Type 2 $\Delta\mathbf{S2}^{\prime\prime\text{tag}}$ are still large and comparable to $\Delta\mathbf{S2}^{\text{tag}}$ (presented in Fig. 18). It is because the cross polarization signals from the proposed scatterer are not as strong as from the dihedral (see Fig. 14).

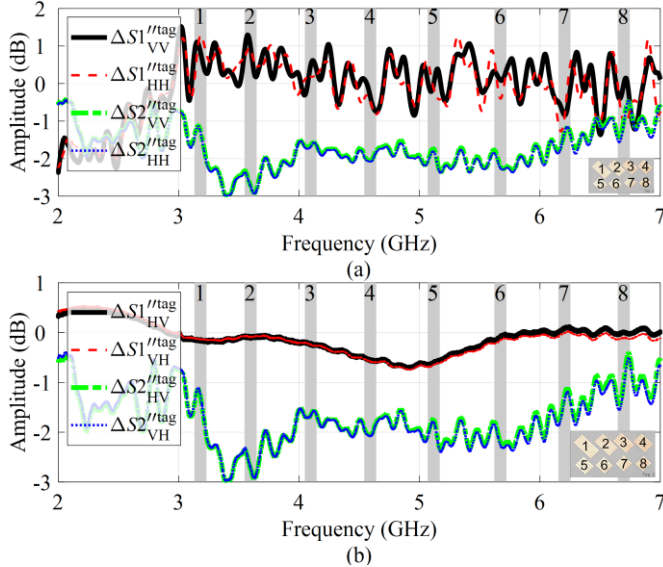


Fig. 19. Calibration error matrix signals $\Delta\mathbf{S1}^{\prime\prime\text{tag}}$ and $\Delta\mathbf{S2}^{\prime\prime\text{tag}}$ for the REP chipless RFID tag as the test target. (a) Co polarization signals. (b) Cross polarization signals. The gray regions show a 100 MHz range around all eight peak apexes of the REP chipless RFID tag.

C. Uncertainty Analyses for the Proposed Calibration Scatterer

The uncertainty analyses for the proposed calibration

scatterer are carried out as illustrated in Fig. 20. A displacement d_x of the rear side of proposed scatterer along H polarization of radar antenna is introduced [see Fig. 20(a)] and the variation of inclination angle θ of the front side of proposed scatterer is applied [see Fig. 20(b)]. For these applied changes, the dihedral tilted at 45° and the REP chipless RFID tag are used as test objects. For ease of observation, only one or two components of scattering matrices are presented. It is important to note that calibration Type 1 is dependent on the displacement d_x of the rear side of proposed scatterer, while the calibration Type 2 is dependent on the inclination angle θ of the front side of proposed scatterer.

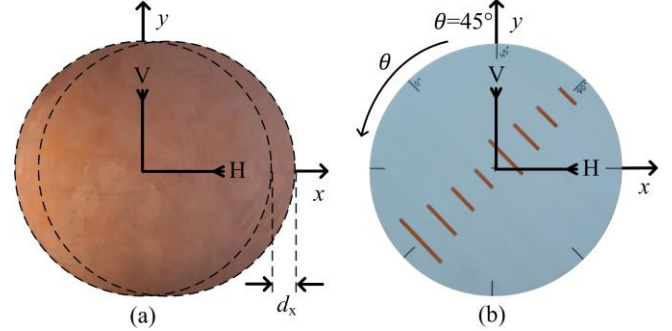


Fig. 20. Illustrations for the uncertainty analyses for the proposed calibration scatterer. (a) Displacement error. (b) Misalignment error.

The displacements on the rear side of proposed scatterer $d_x = [0, 0.6, 1.6, 2.6]$ cm are applied and the radar calibrations are done, where all the parameters and procedures are same as explained in Section VI-B. For d_x ranging from 0 to 2.6 cm, the calibration error signals are presented for the dihedral tilted at 45° and the REP chipless RFID tag in Fig. 21 and Fig. 22, respectively. The effect of d_x on the calibration errors is more pronounced from 5 to 7 GHz. For a small value of displacement $d_x = 0.6$ cm, the calibration errors are approximately the same as the nominal errors at $d_x = 0$. For the dihedral tilted at 45° , the maximum error of $|\Delta\mathbf{S1}_{\text{HV}}^{\text{dih.}(45^\circ)}|$ can reach up to 5.67 dB at $d_x = 2.6$ cm. On the other hand, for the REP chipless RFID tag, the maximum error of $|\Delta\mathbf{S1}_{\text{HH}}^{\text{tag}}|$ and $|\Delta\mathbf{S1}_{\text{VV}}^{\text{tag}}|$ can reach up to 4.44 dB and 3.90 dB, respectively, at $d_x = 2.6$ cm. The proposed scatterer is potentially tolerant of displacement up to 1 cm.

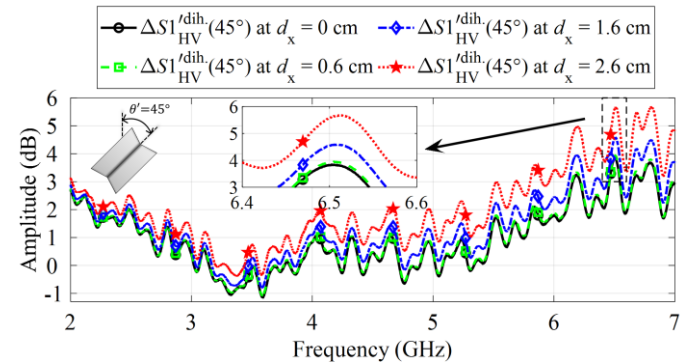


Fig. 21. Calibration error signals $\Delta\mathbf{S1}_{\text{HV}}^{\text{dih.}(45^\circ)}$ for the dihedral tilted at 45° as the test target while d_x is ranging from 0 to 2.6 cm.

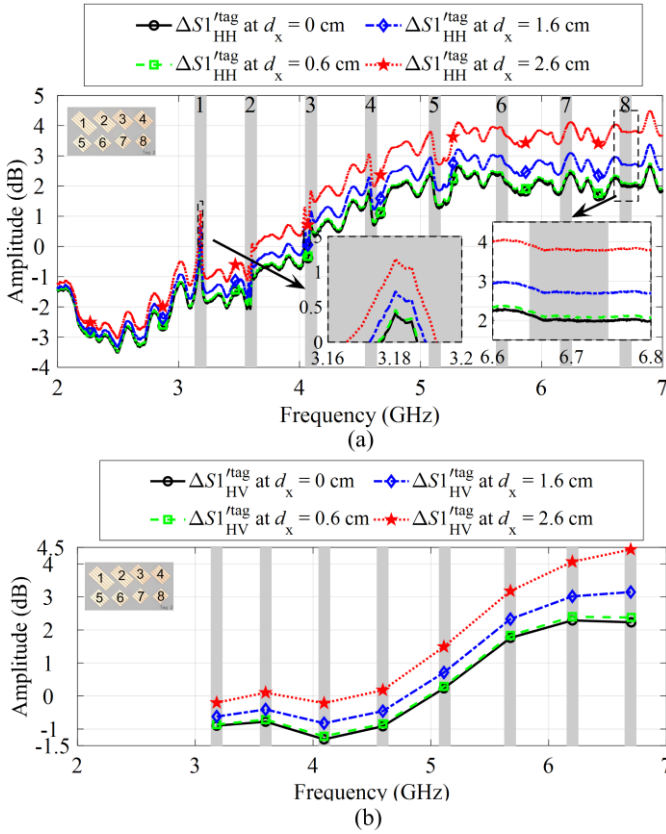


Fig. 22. Calibration error signals for the REP chipless RFID tag as the test target while d_x ranging from 0 to 2.6 cm. (a) Co polarization signals. (b) Cross polarization signals.

The change of inclination angle $\theta = [45^\circ, 47^\circ, 49^\circ]$ is applied on the front side of proposed scatterer and the calibration error signals are calculated. Fig. 23 and Fig. 24 show the calibration error signals for the dihedral tilted at 45° and the REP chipless RFID tag, respectively. With the misalignment d_θ ranging from 0 to 4° , the calibration errors exhibit decreasing and increasing trend from 2 to 4 GHz and 5 to 7 GHz, respectively. For a misalignment $d_\theta = 2^\circ$ (i.e., $\theta = 47^\circ$) the calibration errors are comparable to the nominal errors at $d_\theta = 0$ (i.e., $\theta = 45^\circ$). Therefore, the proposed scatterer is potentially tolerant of misalignment equals 2° .

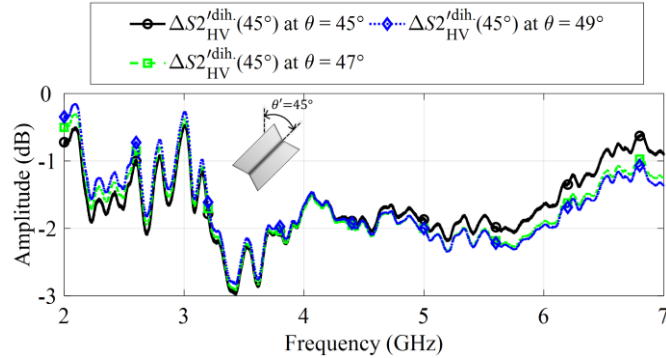


Fig. 23. Calibration error signals $\Delta S_{HV}^{dih}(45^\circ)$ for the dihedral tilted at 45° as the test target while the inclination angles θ is ranging from 45° to 49° .

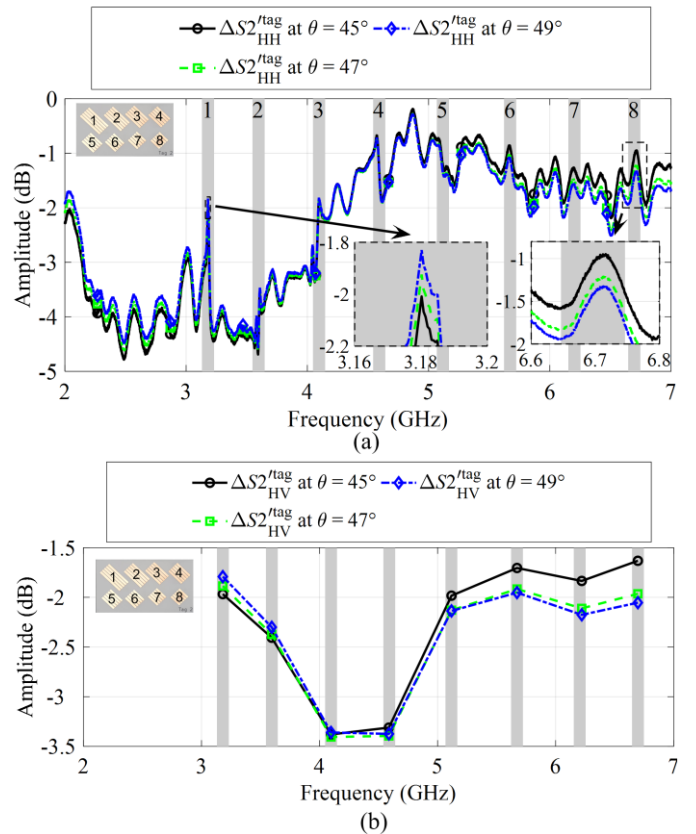


Fig. 24. Calibration error signals for the REP chipless RFID tag as the test target while the inclination angles θ is ranging from 45° to 49° . (a) Co polarization signals. (b) Cross polarization signals.

Finally, the effect of the distance of objects from the radar antenna on the performance of proposed scatterer is analyzed. For this purpose, the distance of the test object, as well as the proposed scatterer, is changed to $d_o = d_c = d_u = 39$ cm. The radar calibration is performed for the dihedral tilted at 45° as the test target and the calibration error signals are calculated with the same procedure as done for the results presented in Fig. 16. Fig. 25 presents the calibration error signals for $d_o = d_c = d_u = 39$ cm $\Delta S_{HV}^{dih}(45^\circ)(39$ cm) and $\Delta S_{HV}^{dih}(45^\circ)(39$ cm) in comparison to the calibration error signals for $d_o = d_c = d_u = 28$ cm $\Delta S_{HV}^{dih}(45^\circ)(28$ cm) and $\Delta S_{HV}^{dih}(45^\circ)(28$ cm) taken from Fig. 16. It can be observed that the $\Delta S_{HV}^{dih}(45^\circ)(39$ cm) and $\Delta S_{HV}^{dih}(45^\circ)(39$ cm) are slight improved as compared to the $\Delta S_{HV}^{dih}(45^\circ)(28$ cm) and $\Delta S_{HV}^{dih}(45^\circ)(28$ cm) (from Fig. 16). The possible reason behind this is with $d_o = d_c = d_u = 39$ cm the objects are closer to the farfield region. One could say that $d_o = d_c = d_u = 39$ cm should be used in the entire paper as it provides better performance. However, the proposed scatterer is intended for calibration of chipless RFID tags which are not designed to be read at larger distances [18].

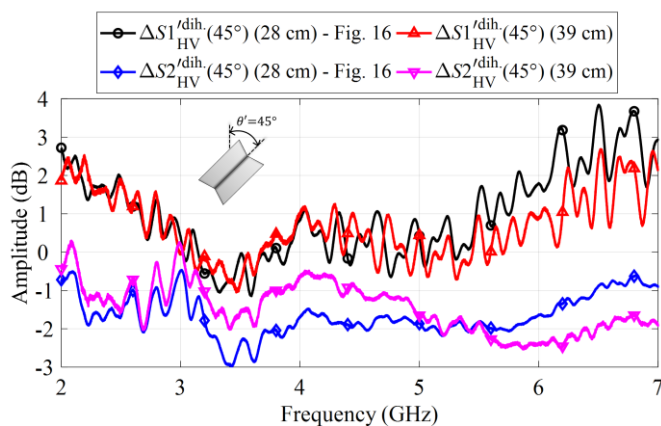


Fig. 25. Calibration error signals $\Delta S1_{HV}^{dih}(45^\circ)$ for the dihedral tilted at 45° as the test target while $d_o = d_c = d_u$ are changed from 28 to 39 cm.

D. Final Remarks

All information regarding the geometrical dimensions, curves of reference used in the calibration process are presented explicitly. This is done to facilitate the readers to use the proposed scatterer in the radar calibration, for example, for chipless RFID.

VII. CONCLUSIONS

In this paper, a low cost, compact and planar circular scatterer is proposed as a radar calibration target that is well suited for chipless RFID. The proposed calibration target is 3-in-1 scatterer: 1) from the rear side, it behaves like a metallic disk; 2) from the front side with vertically aligned dipoles, it behaves like a nondepolarizing scatterer with dominant co polarization backscattered signals; 3) from the front side with 45° tilted dipoles, it behaves like a depolarizing scatterer with strong cross polarization backscattered signals. The proposed scatterer is tested as a reference calibration object for single antenna based polarimetric radar calibration techniques. Two test objects are utilized: a dihedral tilted at 45° and a depolarizing chipless RFID tag. The performance of the proposed scatterer is also compared with the standard reference calibration objects: a metallic disk and a dihedral tilted at 22.5° . It is found that the performance of the proposed scatterer exhibits a good agreement with the standard reference calibration objects. Uncertainty analyses that include displacement, misalignment, and distance are done for the proposed scatterer. The proposed scatterer is potentially tolerant of displacement up to 1 cm and misalignment equals 2° .

REFERENCES

- [1] B. M. Welsh, B. M. Kent, and A. L. Buterbaugh, "Full polarimetric calibration for radar cross-section measurements: performance analysis," *IEEE Trans. Antennas Propag.*, vol. 52, no. 9, pp. 2357–2365, 2004.
- [2] J. -. J. Gau and W. D. Burnside, "New polarimetric calibration technique using a single calibration dihedral," *IEE Proc. Microw. Antennas Propag.*, vol. 142, no. 1, pp. 19–25, 1995.
- [3] C. Beaudoin, T. Horgan, G. Demartinis, M. J. Coulombe, A. J. Gatesman, and W. E. Nixon, "Fully Polarimetric Bistatic Radar Calibration With Modified Dihedral Objects," *IEEE Trans. Antennas Propag.*, vol. 66, no. 2, pp. 937–950, 2018.

- [4] K. Sarabandi, F. T. Ulaby, and M. A. Tassoudji, "Calibration of polarimetric radar systems with good polarization isolation," *IEEE Trans. Geosci. Remote Sens.*, vol. 28, no. 1, pp. 70–75, 1990.
- [5] S. H. Yueh, J. A. Kong, and R. T. Shin, "Calibration of Polarimetric Radars Using in-Scene Reflectors," *Progress In Electromagnetics Research*, vol. PIER 03, pp. 451–510, 1990.
- [6] M. W. Whitt, F. T. Ulaby, P. Polatin, and V. V. Liepa, "A general polarimetric radar calibration technique," *IEEE Trans. Antennas Propag.*, vol. 39, no. 1, pp. 62–67, 1991.
- [7] C. Uluisik, G. Cakir, M. Cakir, and L. Sevgi, "Radar cross section (RCS) modeling and simulation, part 1: a tutorial review of definitions, strategies, and canonical examples," *IEEE Antennas Propag. Mag.*, vol. 50, no. 1, pp. 115–126, 2008.
- [8] C. J. Bradley *et al.*, "An investigation of bistatic calibration objects," *IEEE Trans. Geosci. Remote Sens.*, vol. 43, no. 10, pp. 2177–2184, 2005.
- [9] A. Olk, K. Ben Khadhra, and T. Spielmann, "Highly accurate fully-polarimetric radar cross section facility for mono- and bistatic measurements at W-band frequencies," in *Proc. Antenna Measurement Techniques Association Symposium (AMTA)*, Atlanta, Georgia, 2017, pp. 1–6.
- [10] H. KANG and C. HU, "A method for polarization scattering parameter measurement and calibration based on vector network analyzer," *The Journal of China Universities of Posts and Telecommunications*, vol. 20, pp. 117–120, 2013.
- [11] E. Perret, *Radio Frequency Identification and Sensors: From RFID to Chipless RFID*. Hoboken, NJ, USA: Wiley: Wiley, 2014.
- [12] O. Rance, E. Perret, R. Siragusa, and P. Lemaître-Auger, *RCS Synthesis for Chipless RFID: Theory and Design*. Elsevier, 2017.
- [13] W. Wiesbeck and S. Riegger, "A complete error model for free space polarimetric measurements," *IEEE Trans. Antennas Propag.*, vol. 39, no. 8, pp. 1105–1111, Aug. 1991.
- [14] "Datasheet - Open Boundary Quad-Ridge Horns." MVG, 2019, Accessed: Nov. 20, 2020. [Online]. Available: <https://www.mvg-world.com/en/products/antennas/measurement-probes-and-feeds/open-boundary-quad-ridge-horns>.
- [15] M. Svanda, M. Polivka, J. Havlicek, J. Machac, and D. H. Werner, "Platform Tolerant, High Encoding Capacity Dipole Array-Plate Chipless RFID Tags," *IEEE Access*, vol. 7, pp. 138707–138720, 2019.
- [16] D. M. Pozar, *Microwave Engineering*, 2nd ed. New York, USA: Wiley, 1998.
- [17] E. F. Knott, "RCSR Guidelines Handbook," Georgia Institute of Technology, Engineering Experiment Station, Atlanta, Georgia, Report on Contract N00039–73-C-0676 Defense Technical Information Center No. AD A099566, 1976. [Online]. Available: <https://apps.dtic.mil/dtic/tr/fulltext/u2/a099566.pdf>.
- [18] A. Vena, E. Perret, and S. Tedjni, "A Depolarizing Chipless RFID Tag for Robust Detection and Its FCC Compliant UWB Reading System," *IEEE Trans. Microw. Theory Techn.*, vol. 61, no. 8, pp. 2982–2994, Aug. 2013.
- [19] G. T. Ruck, D. E. Barrick, and W. D. Stuart, *Radar Cross Section Handbook*, vol. 1, 3 vols. Newport Beach, CA, USA: Peninsula Publishing, 2002.
- [20] E. F. Knott, *Radar Cross Section Measurements*. New York, USA, 1993.